Title

Monitoring osseointegrated prosthesis loosening and fracture using electrical capacitance tomography.

Journal

Biomedical engineering letters, 8(3)

ISSN

2093-9868

Authors

Gupta, Sumit
Loh, Kenneth J

Publication Date

2018-08-01

DOI

10.1007/s13534-018-0073-4

Peer reviewed

Monitoring Osseointegrated Prosthesis Loosening and Fracture using Electrical Capacitance Tomography

Sumit Gupta[1] and Kenneth J. Loh[1*]

[1]Department of Structural Engineering, University of California-San Diego, La Jolla, CA, 92093-0085, USA

[*]Corresponding author, email: kenloh@ucsd.edu

Abstract

A noncontact, noninvasive, electrical permittivity imaging technique is proposed for monitoring loosening of osseointegrated prostheses and bone fracture. The proposed method utilizes electrical capacitance tomography (ECT), which employs a set of noncontact electrodes, arranged in a circular fashion around the imaging area, for electrical excitations and measurements. An inverse reconstruction algorithm was developed and implemented to reconstruct the electrical permittivity distribution of the interrogated region from boundary capacitance measurements. In this study, osseointegrated prosthesis phantoms were prepared using plastic rods and Sawbone femur specimens, which were subjected to prosthesis loosening and fracture monitoring tests. The results demonstrated that the spatial location and extent of prosthesis loosening and bone fracture could be estimated from the ECT reconstructed permittivity maps. The resolution of the reconstructed images was further enhanced by a limited region tomography algorithm, and its accuracy in terms of identifying the severity, location, and shape of bone fracture was also investigated and compared with conventional full region tomography.

Keywords

Electrical capacitance tomography, electrical permittivity, fracture, noncontact, osseointegrated prosthesis, prosthesis loosening.

Introduction

Prosthetic technologies and its recent advancements have helped amputees tremendously in terms of regaining their quality of life and day-to-day functionalities prior to limb loss. Although, socket-based prostheses remain most common and are widely used, osseointegrated prostheses (OIP) are becoming more popular, since discomfort caused by the constant contact between the residual stump and socket prosthesis, which can lead to skin irritations and pressure ulcers, would no longer be an issue. Furthermore, amputees with OIP have reported improved sensory feedback (*i.e.*, osseo-perception) and improved sitting comfort with reduced soft-tissue problems [1].

Despite these aforementioned benefits, failed osseointegration post-surgery and prosthesis loosening remain major issues. They can occur due to excessive motion and physical stress during rehabilitation or, thereafter, increased shear force at the tissue-prosthesis interface due to misalignment, stress-shielding-related peri-prosthetic bone loss, mineralization defect, and infections, to name a few [2]. Failure of early assessment of prosthesis loosening can result in further complications, such as complete disbonding and bone fracture, which necessitates revision surgery and implant replacement.

Besides regular clinical visits, different nuclear scanning techniques (*e.g.*, computed tomography (CT), positron emission tomography (PET), bone scintigraphy, single photon emission computed tomography (SPECT), and magnetic resonance imaging (MRI)) remain the most common, reliable, and accurate diagnostic tools for detecting prosthesis loosening [3, 4]. An advantage of MRI, CT, and PET is their ability to produce 3D images. Bone scintigraphy can also be used for characterization of bone metabolism. However, many of these imaging techniques require radiation, which is harmful at high doses. In addition, the radiation used sometimes induces bone loss at the

bone-OIP interface [5]. Artifacts due to the presence of metallic implants are also a well-known problem in cross-sectional imaging (*e.g.*, in the case of MRI). Beside these aforementioned nuclear scanning tests, ultrasonic imaging technique is regarded as one of the most widely used and low-cost non-nuclear scanning techniques for peri-prosthetic assessment. However, its accuracy depends on its operator. In some cases, it also fails to detect the exact location of abnormalities [4].

Therefore, this study presents a noncontact, portable, non-radiation-based imaging technique that can be used to detect the onset of and diagnose prosthesis loosening, as well as loosening-induced bone fractures. The proposed method works on the principle of electrical capacitance tomography (ECT), where the electrical permittivity distribution of a predefined sensing area can be reconstructed from a limited number of noncontact capacitance measurements obtained at the boundary of the sensing area. Since bone and metallic prostheses are characterized by drastically different electrical permittivity, it is hypothesized that ECT can map changes in electrical permittivity and detect dislocation and loosening of the OIP. In addition, loosening-induced bone fracture can also be identified and localized using ECT. This letter begins with a brief description of the ECT formulation, followed by the test protocols and corresponding laboratory validation results.

ECT Background

As mentioned earlier, ECT was employed in this study to estimate the change in spatial permittivity distribution due to prosthesis loosening and bone fracture. In fact, ECT is a well-established technique and has been investigated for monitoring various industrial processes [6-8]. However, ECT has not been widely utilized for imaging the human body, and the main contribution of this work is to demonstrate its potential for biomedical applications. In short, ECT works by propagating an alternating current (AC) signal through a predefined sensing area, and the capacitance between pairs of boundary electrodes are measured during ECT interrogation and data acquisition. This raw dataset is then used as inputs to solve the ECT inverse problem and to reconstruct the permittivity distribution of the sensing area [9]. Similar to CT, which is widely used for medical imaging, cross-sectional images of the human body can be obtained; however, a distinct difference is that ECT employs low-amplitude electric field excitations in lieu of harmful radiation.

In this study, the ECT sensing region is a 2D circular area circumscribed by eight boundary electrodes equidistantly spaced from one another. Central to the ECT algorithm is the 2D Laplace's equation:

$$\nabla \cdot (\varepsilon \nabla u) = 0 \tag{1}$$

where ε is the permittivity distribution of the sensing area, and u is electrical potential distribution. If permittivity distribution is known *a priori*, the 2D Laplace's equation can be solved with the aid of finite element modeling (FEM) to estimate the boundary capacitance responses for a given electrical field excitation; this is referred to as the forward problem.

From an experimental standpoint, the ECT inverse problem needs to be solved. Here, a high-speed capacitance measurement unit (CMU) is employed to measure the capacitance (C_m) between boundary electrode pairs when an electrical field is excited from one electrode while all other electrodes are grounded. This data is then used as inputs to the ECT algorithm.

To solve the inverse problem, the ECT forward problem is solved using an assumed permittivity distribution (ε) to calculate the corresponding boundary capacitance responses (C_c). The error norm between C_m and C_c is minimized to obtain the unknown permittivity distribution from C_m. In order to handle the ill-posed nature of the ECT inverse problem, an appropriate regularization technique should be implemented by adding a penalty term to the cost function (p), as shown in equation (2).

$$p = \arg\min \left[\| C_m - C_c \| \right]^2 + \alpha^2 \| R(\varepsilon - \varepsilon_b) \|^2 \tag{2}$$

where α is the regularization parameter, R is the regularization matrix, and ε_b is the assumed background electrical permittivity distribution. In this study, total variation (TV) regularization technique was adopted, and a Gauss-Newton algorithm was implemented to iteratively minimize p. The permittivity distribution was updated after each iteration, and the forward problem was solved to estimate a new boundary capacitance response based on the corresponding

permittivity distribution. This procedure was repeated until the ratio of the norm of the difference between C_m and C_c with respect to C_m reached a predefined threshold limit of 0.05%. More details of the ECT inverse problem can be found in the previous work by Gupta and Loh [10].

Experimental Details

1. Prosthesis loosening monitoring

The first set of experiments was performed to validate that ECT could detect OIP loosening. Instead of performing an *in vivo* test, an OIP surrogate was prepared and used for this preliminary study, where a 12.8 mm-diameter poly(vinyl chloride) (PVC) rod was slipped into the medullary cavity of a Sawbone femur. A previous study already demonstrated that ECT can accurately reconstruct the permittivity distribution of actual tissue-and-bone specimens, as well as Sawbone with metallic OIPs [11]. A PVC OIP surrogate was chosen as a more challenging environment for spatial permittivity reconstruction, since the electrical permittivity of PVC is considerably less than that of metal and more comparable to bone.

For this test, the entire surrogate was placed in the central region of the ECT electrode array as shown in Fig. 1a. The prosthesis was gradually pulled out from the medullary cavity starting from 0 mm to 35 mm, and at 5 mm increments, to simulate the effects of prosthesis loosening (Fig. 1b). At the end of each 5 mm movement, the system was interrogated by the ECT system, and the corresponding electrical permittivity distributions were reconstructed from the measured set of boundary capacitance responses.

2. Fracture detection at bone-prosthesis interface

As mentioned earlier, prosthesis loosening, if undetected at an early stage, can cause stress concentrations in bone and, ultimately, cracks (or fracture) can propagate at the bone-prosthesis interface, thereby leading to OIP failure and extreme pain for the amputee. Thus, the second experiment aims to investigate whether ECT can be applied as a noninvasive imaging tool to detect the location and severity of cracks at the bone-prosthesis interface. Similar to the previous test surrogate, a Sawbone femur was selected. Instead of a plastic rod, an aluminum rod that is 12.8 mm in diameter was inserted into the medullary cavity to create the OIP surrogate. To ensure a secure fit, quick-setting epoxy was employed to bond the metal rod with the femur replica. A side- and top-view of the surrogate can be seen in Figs. 2a and 2b, respectively. A slit (*i.e.*, ~ 3 mm deep and ~ 3 mm wide) was then cut along the side and in the direction of the longitudinal axis of the femur using a Dremel tool, as shown in Figs. 2c and 2d, for emulating fracture. Thereafter,

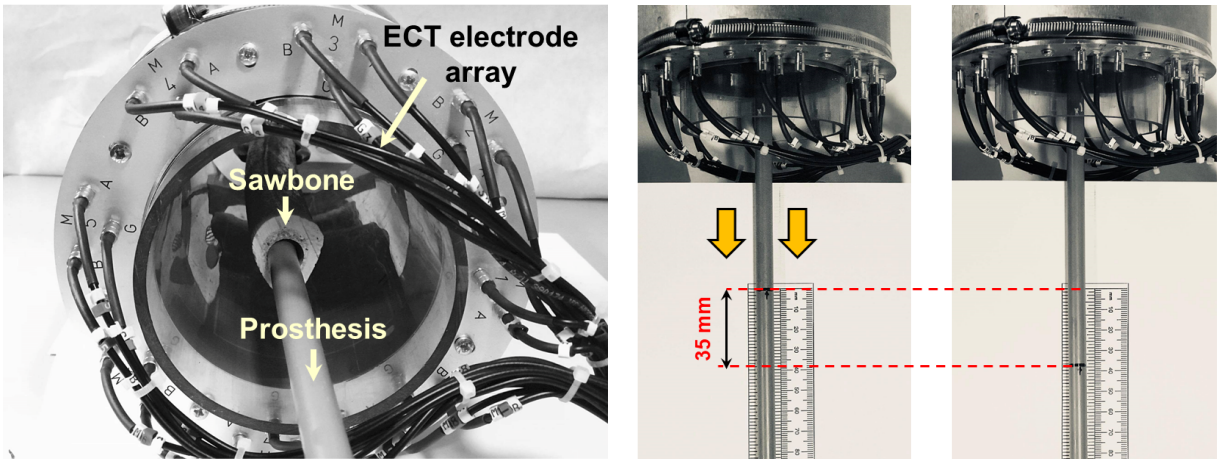

(a) (b)

Fig.1. (a) Prosthesis loosening monitoring tests were conducted using a bone-prosthesis phantom by placing it near the center of the ECT electrode array for interrogation. (b) The prosthesis phantom was gradually pulled out from Sawbone femur, while ECT measurements were recorded.

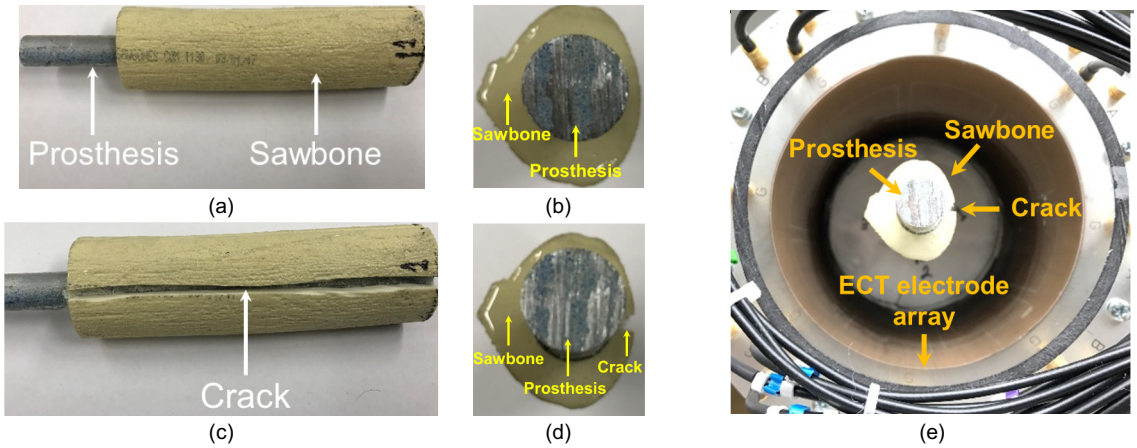

Fig. 2. An aluminum rod was inserted in a Sawbone femur to create the OIP surrogate, and (a) its longitudinal and (b) cross-sectional views are shown. (c) A longitudinal cut is made along the side of the Sawbone, and (d) its cross-section is also shown. (e) The OIP surrogate was placed in the center of the ECT electrode array for ECT interrogation and data acquisition.

the surrogate was placed at middle of the ECT electrode array for ECT interrogation and data acquisition as shown in Fig. 2e.

After validating that ECT could detect fracture location at the bone-prosthesis interface, additional tests were performed to see if ECT can also be used to quantify fracture size (*i.e.*, its length and depth). Like the previous fracture detection test, similar experimental procedures were followed. Here, a 12.8 mm-diameter PVC rod was employed for the rest of this study. A slit (*i.e.*, ~ 14 mm deep and ~ 3 mm wide) was cut using a Dremel tool along the longitudinal axis of the OIP surrogate as shown in Fig. 3a. The length of the fracture was gradually increased from 5 mm to 30 mm in 5 mm increments. After each increment in fracture length, ECT measurements were recorded for spatial permittivity reconstruction. In order to accurately maintain the position of the OIP surrogate in the ECT electrode array (*i.e.*, during removal of the OIP surrogate for cutting), a ProMatte fixture was printed using a Type A Series 1 Pro 3D printer. This receptacle was placed at the bottom of the ECT electrode array, and the OIP surrogate was inserted into the middle slot in the ECT electrode array as shown in Fig. 3b.

Finally, the depth of the fracture was quantified using a similar experimental setup as before. Here, a 35 mm-long slit was cut along the longitudinal axis of the OIP surrogate. The depth of the fracture was gradually increased from its pristine and undamaged state to 14.25 mm in ~ 2.85 mm increments. ECT measurements were obtained after each additional ~ 2.85 mm increment of depth in cut.

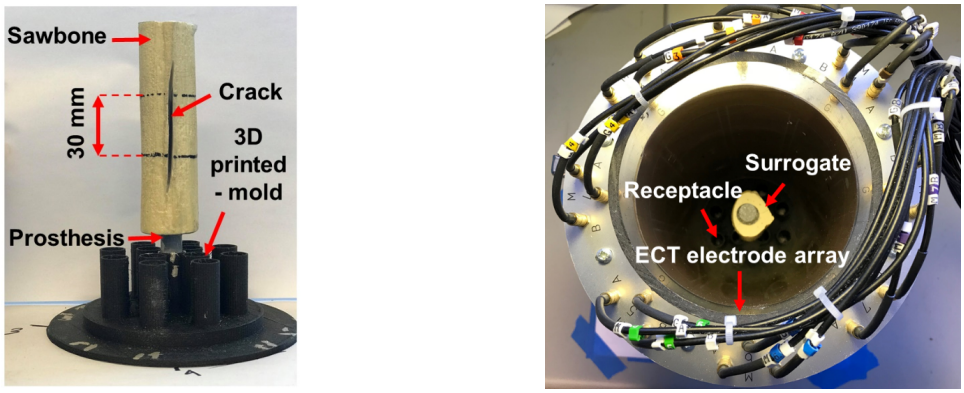

Fig. 3. (a) The OIP surrogate was inserted in a 3D-printed mold to maintain its position in the ECT electrode array during imaging. (b) The 3D-printed mold was placed at the bottom of the ECT electrode array, and the entire test setup is shown.

ECT Image Evaluation Criteria

Two image parameters were evaluated and used to characterize the quality of reconstructed images. The image parameters were evaluated on the basis of the one-fourth amplitude set or $[\varepsilon_q]_i$, which contains all the image pixels greater than one-fourth of the maximum amplitude of all the image pixels ($[\varepsilon]_i$) as defined by Adler *et al.* [12]. Mathematically, the one-fourth amplitude set is defined by equation (3).

$$[\varepsilon_q]_i = \begin{cases} 1 \text{ if } [\varepsilon]_i \geq 1/4 \max[\varepsilon] \\ 0 \text{ otherwise} \end{cases} \tag{3}$$

where $[\varepsilon]$ is the reconstructed permittivity distribution. By setting the threshold to one-fourth of the maximum amplitude of permittivity change, most of the visually significant effects were taken into consideration for qualitative assessment of the reconstructed permittivity maps [12]. Position error (*PE*) was then evaluated by calculating the distance between the center-of-gravity (CG) of the defects (*e.g.*, bone fracture and prosthesis loosening) and $[\varepsilon_q]_i$.

$$PE = | r_t - r_q | \tag{4}$$

where r_t and r_q are the position vectors of the CG of the defects and $[\varepsilon_q]_i$, respectively. *PE* measures how accurately the reconstructed images could identify the location of the defects, where smaller values of *PE* signify higher accuracy of the reconstructed image. Then, area ratio (*AR*) is defined as the fraction of the area of all the pixels of $[\varepsilon_q]_i$ located in the damaged region with respect to the actual damage size (*D*).

$$AR = \sum_{i \in D} [\varepsilon_q]_i / D \tag{5}$$

AR represents the accuracy of the reconstructed images in terms of its ability to identify the shape and size of defects, where *AR* values close to 1 represent a higher-quality image.

Results and Discussion

1. Prosthesis loosening results

As stated earlier, ECT was employed for monitoring OIP loosening. Fig. 4 shows the change in relative permittivity distributions acquired at different stages of displacement of the prosthesis phantom as it was gradually pulled out from 5 mm to 35 mm. It should be mentioned that the results in Fig. 4 plot the change in electrical permittivity distribution with respect to the initial or pristine (*i.e.*, 0 mm) specimen's permittivity distribution. A baseline was used in this case to highlight changes in relative permittivity due to prosthesis loosening. First, it is clear that ECT can successfully identify the location of permittivity changes due to loosening of the prosthesis. Second, a decrease in electrical permittivity was observed with increasing pull-out, because the pulled-out section or void was filled with air, which has a lower permittivity than the PVC rod. The magnitude of permittivity change was smaller at initial stages of prosthesis pull-out, because a portion of the prosthesis rod was still within the interrogating electric field. As the prosthesis phantom was loosened further, a large decrease in electrical permittivity was observed as expected.

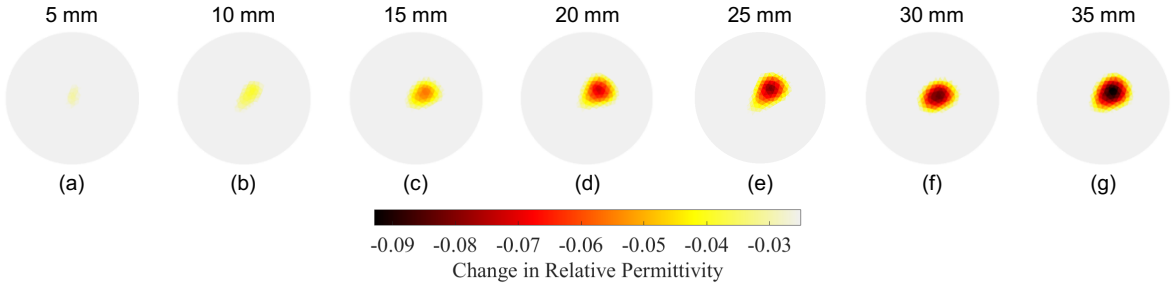

Fig. 4. Relative permittivity distributions due to prosthesis loosening at different loosening states were reconstructed and compared to the baseline (*i.e.*, undamaged state). ECT results corresponding to OIP pull-out of (a) 5, (b) 10, (c) 15, (d) 20, (e) 25, (f) 30, and (g) 35 mm are shown.

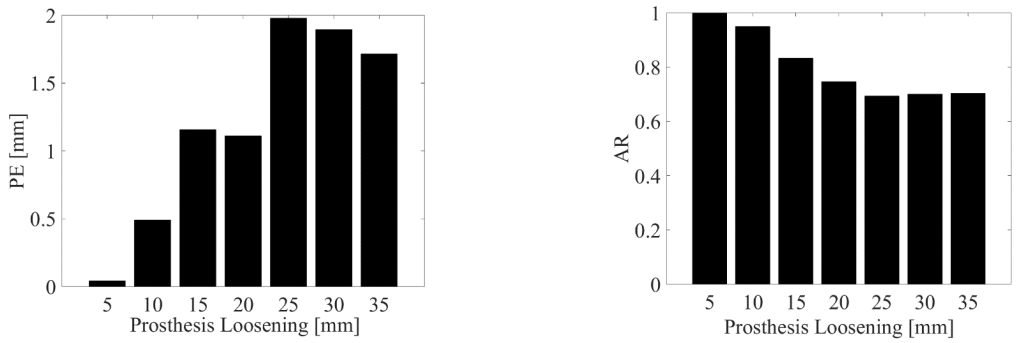

(a) (b)

Fig. 5. The ECT image resolution criteria, namely (a) *PE* and (b) *AR*, were evaluated for the reconstructed images corresponding to different extents of OIP pull-out.

After successfully detecting the location and extent of prosthesis loosening, *PE* and *AR* were evaluated for assessing the quality of the reconstructed ECT images. First, the maximum change in electrical permittivity was found among all of the reconstructed images and used for defining the one-fourth amplitude set. Second, in order to calculate *PE* and *AR*, it was assumed that the center of the OIP surrogate coincided with the center of the ECT electrode array (which, according to Fig. 1a, was a reasonable assumption). Although *PE* was smaller than ~ 2 mm, it was found that it increased after the first 5 mm of OIP pull-out. In contrast, it was found that *AR* was ~ 1 during the first 5 mm of pull-out, and its value gradually decreased from ~ 1 to ~ 0.7. For both of these criteria, accuracy seemed to deteriorate with greater pull-out. This could be due to the reason that the OIP surrogate was displaced from the center of the ECT electrode array after initial pull-out, thus increasing experimental error. Overall, accuracy and resolution seemed reasonable, especially considering that the size of each ECT electrode and that the ECT system only used eight boundary electrodes. Future studies will consider larger number of electrodes for enhancing imaging performance.

2. Bone fracture detection validation

In the second part of this study, a fracture was introduced by cutting a slit in the Sawbone at the bone-prosthesis interface, and the surrogate was subjected to ECT testing. It should be mentioned that this test involved obtaining two different baseline permittivity maps of the sensing region. The first was the permittivity distribution of an empty ECT sensing region (*i.e.*, with only air). The second was obtained by interrogating the pristine or undamaged surrogate when placed at the center of the ECT electrode array. Fig. 6a shows the electrical permittivity distribution of the pristine OIP surrogate, and the change in permittivity was calculated with respect to the baseline of an empty sensing region. Fig. 6b shows the permittivity distribution of the fractured OIP surrogate (*i.e.*, with respect to the undamaged case shown in Fig. 6a). It can be observed from Fig. 6b that a sharp decrease in electrical permittivity was observed near the vicinity of the area where the crack was located. This result makes sense, since fracture (*i.e.*, bone loss)

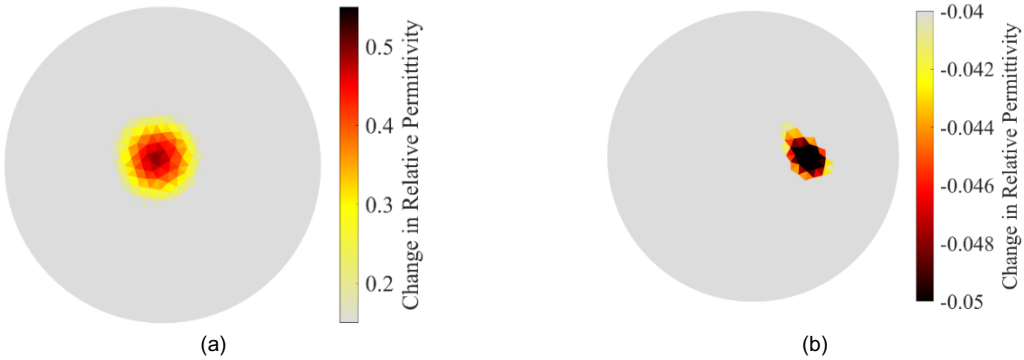

(a) (b)

Fig. 6. (a) The permittivity distribution corresponding to the pristine OIP surrogate was reconstructed, and the change in relative permittivity with respect to an empty electrode array is shown. (b) The change in permittivity distribution due to the introduction of a fracture in the Sawbone femur (taken with respect to the pristine case) is shown.

corresponds to the creation of a void (or air) at the location of fracture. Since air has a lower electrical permittivity than Sawbone, the permittivity maps show a decrease in permittivity.

3. Monitoring bone fracture length

The next set of experiments aimed to detect the longitudinal growth of a fracture along the length of the Sawbone and OIP surrogate. Similar to the previous test, changes in permittivity due to increases in fracture length was compared to that of the undamaged state, and the results are shown in Fig. 7. It can be noticed that the ECT results showed a decrease in electrical permittivity corresponding to the location of the fracture. The absolute magnitude of permittivity change increased in tandem with increasing fracture length (*i.e.*, from 0 mm to 30 mm). Fig. 8 summarizes the results of Fig. 7 and plots the maximum change in permittivity of each ECT result in Fig. 7 with respect to crack length. It can be seen from Fig. 8 that the maximum change of electrical permittivity continued to decrease, in an approximately linear fashion, as the length of the fracture increased.

After successfully detecting the location and extent of bone fracture along the length of the OIP surrogate, *PE* and *AR* were evaluated, and the results are summarized in Fig. 9. It should be mentioned that the OIP surrogate was removed from the ECT electrode array each time to increase crack length and was then placed back into the sensing region, which undoubtedly would introduce some experimental error. It can be seen from Fig. 9a that *PE* varied seemingly randomly, which could be due to position mismatch every time the OIP surrogate was removed and replaced. On the other hand, the results for *AR* were more consistent. Initially, the crack was just ~ 5 mm, and it was located far away from the center of the plane of ECT boundary electrodes; as a result, *AR* was comparatively small (~ 0.8). However, as crack length was gradually increased, *AR* reached a value closer to 1 (*i.e.*, ~ 0.97).

4. Monitoring bone fracture depth

As mentioned earlier, the last set of ECT experiments was performed to monitor changes in fracture depth occurring at the bone-prosthesis interface. In this case, fracture depth was gradually increased, by sawing the bone using a Dremel tool, from its initial pristine state to ~ 14.25 mm in depth. The electrical permittivity distributions of different

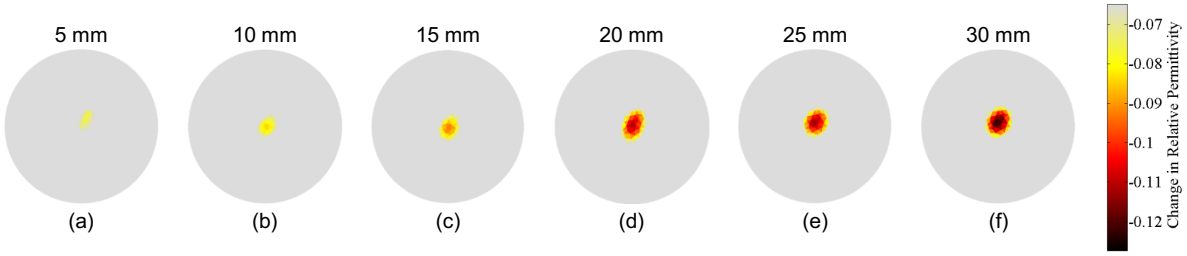

Fig. 7. The change in relative permittivity distributions due to the gradual increase in fracture length along the length of the Sawbone femur, starting from (a) 5, (b) 10, (c) 15, (d) 20, (e) 25, to (f) 30 mm, are shown.

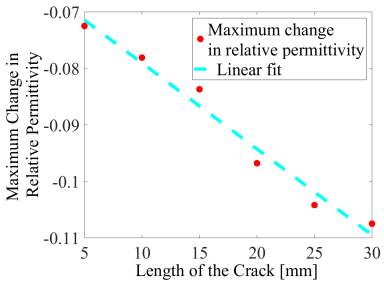

Fig. 8. The maximum change in relative permittivity of the ECT results for cases of a longitudinal fracture of different lengths (5 mm to 30 mm) are plotted.

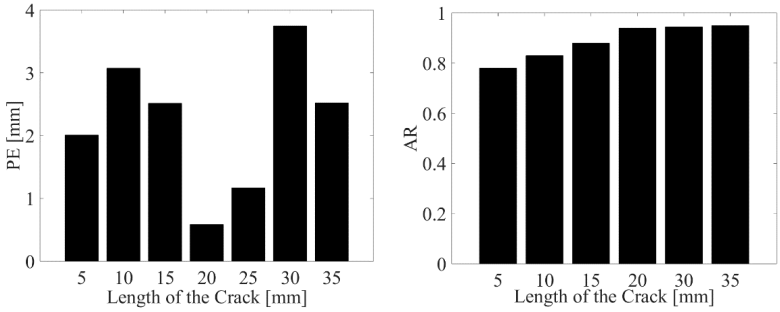

(a) (b)

Fig. 9. (a) *PE* and (b) *AR* were evaluated using the reconstructed ECT images corresponding to different bone fracture lengths.

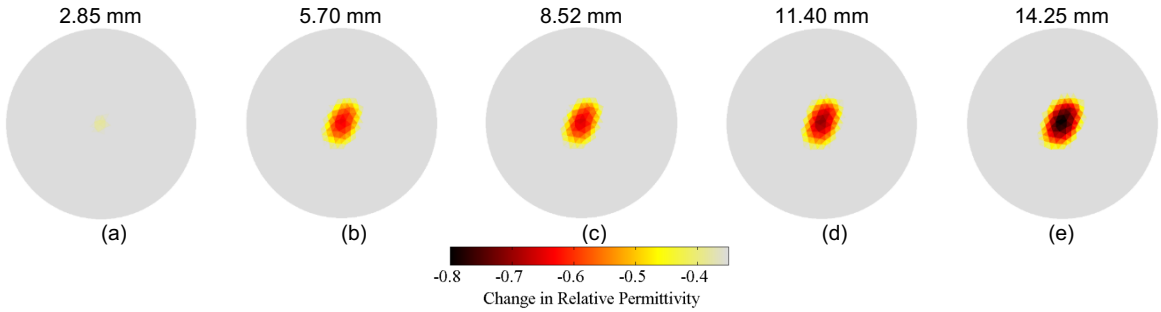

Fig. 10. A ~ 35 mm-long fracture was introduced along the longitudinal direction of the OIP surrogate, and its depth was gradually increased from its pristine state to ~ 14.25 mm at ~ 2.85 mm increments. The corresponding changes in electrical permittivity distribution with respect to the pristine state are shown for (a) 2.85, (b) 5.70, (c) 8.52, (d) 11.40, and (e) 14.25 mm, respectively.

fracture states (*i.e.*, changes in electrical permittivity with respect to the pristine OIP surrogate) are shown in Fig. 10. Although ECT was able to successfully capture the location and gradual changes in electrical permittivity due to the increase in fracture depth, it was observed that fracture size was overestimated, especially since the ECT results showed a decrease in electrical permittivity over a larger area than the actual size of the fracture. This undesirable effect was likely due to the inherent smoothing effect of the regularization technique employed during solving of the inverse problem. Furthermore, the reconstructed images also suffered from poor resolution, where the exact shape and size of the fracture were not clearly identified.

5. ECT image reconstruction enhancement

In order to overcome the aforementioned shortcomings concerning ECT image accuracy and resolution, a limited region tomographic (LRT) image reconstruction algorithm was developed and implemented [13, 14]. Only the region corresponding to the area of the Sawbone was reconstructed to monitor fracture propagation near the bone-prosthesis interface. Fig. 11a describes the dimensions of the "limited region" considered (*i.e.*, the area surrounding the OIP surrogate). The main objective of LRT was to enhance imaging performance of the inverse algorithm by limiting the reconstruction region to a particular zone where changes in electrical permittivity were expected to occur. In doing so, the number of unknown image pixels could be significantly reduced with LRT imaging, thereby reducing the ill-posed-ness of the inverse problem as compared to conventional full region tomography (FRT) image reconstruction algorithms.

For the ECT sensing region considered in this study (Fig. 11a), the original FEM mesh constituted 4,020 linear triangular elements (Fig. 11b), among which 393 were used for LRT reconstruction (Fig. 11c). Using the same sets of data as those presented in Fig. 10, the LRT algorithm was employed for reconstructing high-resolution ECT images, which are shown in Fig. 12. First, it can be observed from Fig. 12 that the ECT results are of visually higher resolution

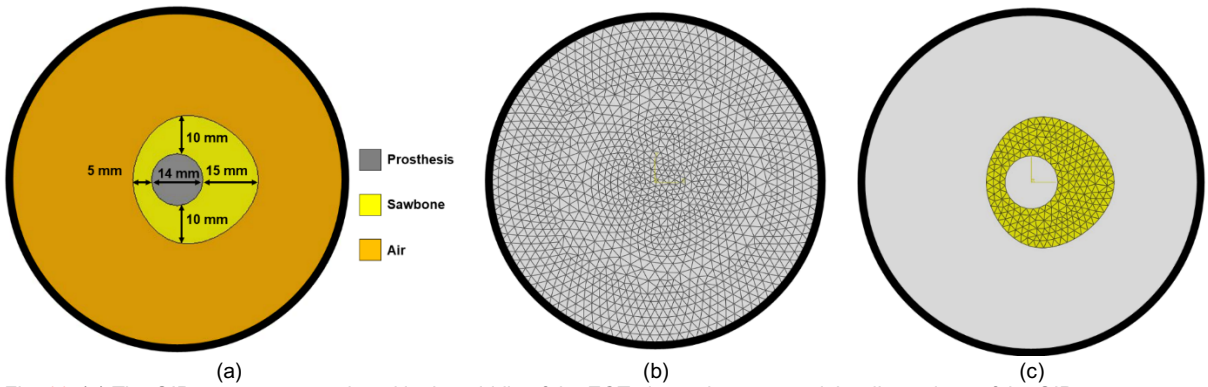

Fig. 11. (a) The OIP surrogate was placed in the middle of the ECT electrode array, and the dimensions of the OIP surrogate are shown. (b) The entire ECT electrode array was modeled by FEM and discretized using linear triangular element. (c) The elements corresponding to the OIP surrogate was considered for image reconstruction by LRT.

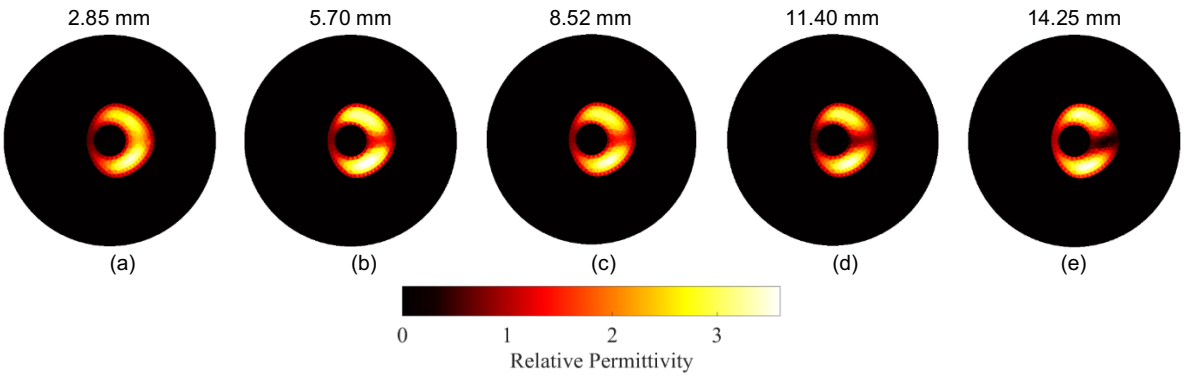

Fig. 12. Electrical permittivity distributions corresponding to different crack depths (*i.e.*, (a) 2.85, (b) 5.70, (c) 8.52, (d) 11.40, and (e) 14.25 mm) obtained by solving the LRT algorithm are shown.

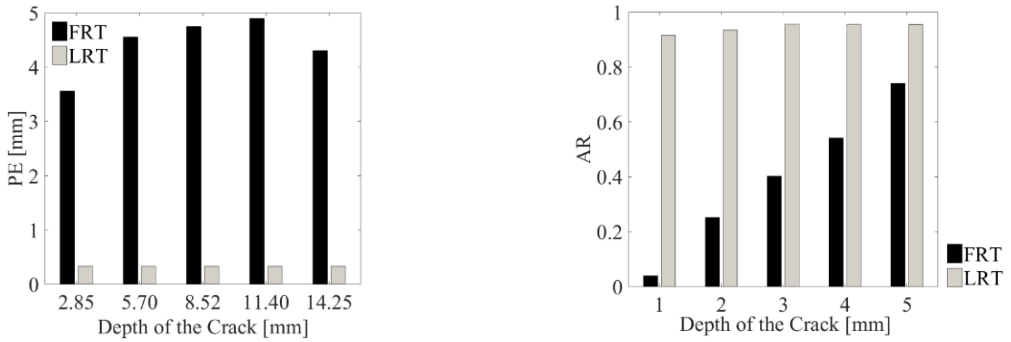

(a) (b)

Fig. 13. The advantages of LRT were clearly demonstrated by comparing (a) *PE* and (b) *AE* values for LRT and FRT images corresponding to different fracture depths.

and accuracy as compared to Fig. 10. Second, gradual shape changes in the reconstructed electrical permittivity maps were observed near the location of the fracture, and these corresponded to the depth of the fracture increasing. Finally, the shape of the change in electrical permittivity also resembled the actual cross-sectional shape of the fracture. In this case, *PE* and *AR* were calculated and compared to the FRT ECT images (*i.e.*, Fig. 10), and the results are summarized in Fig. 13. It can be observed from Fig. 13a that, by using LRT, *PE* was significantly reduced to ~ 0.45 mm from ~ 5 mm. Fig. 13b shows that the LRT images yielded an *AR* of ~ 1 for all fracture depths. Overall, the conclusion is that LRT can be used to generate accurate, high-resolution, ECT images for detecting the shapes and sizes of fractures occurring near the bone-prosthesis interface.

Conclusions

In this study, a noncontact, noninvasive, electrical permittivity imaging technique was proposed for monitoring osseointegrated prosthesis loosening and bone fracture occurring near the bone-prosthesis interface. Several laboratory-based tests were performed using OIP surrogates made using plastic or metallic rods and Sawbone femurs. First, prosthesis loosening tests were performed by gradually pulling out the OIP surrogate from the Sawbone while ECT interrogated the system. The change in dielectric property (*i.e.*, electrical permittivity) due to prosthesis loosening was successfully captured by ECT. Second, ECT was also applied for detecting and monitoring bone fracture propagation near the bone-prosthesis interface. The results showed that ECT was able to detect changes in electrical permittivity due to increases in both the length and depth of fractures. Two image evaluation metrics were defined and used to evaluate the quality of the reconstructed ECT images. Furthermore, to enhance the resolution of the reconstructed images, a limited region tomography algorithm was developed and implemented. The same two metrics were also used to compare the accuracy of the reconstructed images obtained by conventional full region tomography versus LRT for monitoring different bone fracture depths. It was found that the accuracy and resolution of the

reconstructed ECT images can be dramatically enhanced using LRT, where the results correctly identified the shape and depth of longitudinal fractures in the Sawbone. In the near future, actual femur bone specimens and *in vivo* tests will be performed to better characterize the ability of ECT to detect prosthesis loosening and bone fracture in even more realistic conditions.

Acknowledgements

This research was supported by Office of Naval Research (ONR) under grant number N00014-17-1-2550 (program manager: Dr. Liming Salvino). The authors also thank Mr. Han-Joo Lee for his assistance with taking photographs of the experimental setup.

References

1. Sullivan J, Uden M, Robinson KP, and Sooriakumaran S. Rehabilitation of the trans-femoral amputee with an osseointegrated prosthesis: The United Kingdom experience. Prosthetics and Orthotics International. 2003; 27(2): 114-120.
2. Piscitelli P, Iolascon G, Innocenti M, Civinini R, Rubinacci A, Muratore M, D'Arienzo M, Leali PT, Carossino AM, and Brandi ML. Painful prosthesis: approaching the patient with persistent pain following total hip and knee arthroplasty. *C*linical Cases in Mineral and Bone Metabolism. 2013; 10(2): 97-110.
3. Unger AC, Cabrera-Palacios H, Schulz AP, Jürgens C, and Paech A. Acoustic monitoring (RFM) of total hip arthroplasty results of a cadaver study. European Journal of Medical Research. 2009; 14(6): 264-271.
4. Lohmann CH, Rampal S, Lohrengel M, Singh G. Imaging in peri-prosthetic assessment: an orthopaedic perspective. EFORT Open Reviews. 2017; 2(5): 117-25.
5. She C, Shi GL., Xu W, Zhou XZ, Li J, Tian Y, Li WH, Dong QR, and Ren PG. Effect of lowdose Xray irradiation and Ti particles on the osseointegration of prosthetic. *J*ournal of Orthopaedic Research. 2016; 34(10): 1688-1696.
6. Liu S, Chen Q, Wang HG, Jiang F, Ismail I, and Yang WQ. Electrical capacitance tomography for gas–solids flow measurement for circulating fluidized beds. Flow Measurement and Instrumentation. 2005; 16(2):135-144.
7. Warsito W and Fan LS. Measurement of real-time flow structures in gas–liquid and gas–liquid–solid flow systems using electrical capacitance tomography (ECT). Chemical Engineering Science. 2001;56(21): 6455-6462.
8. Xie CG, Huang SM, Beck MS, Hoyle BS, Thorn R, Lenn C, and Snowden D. Electrical capacitance tomography for flow imaging: system model for development of image reconstruction algorithms and design of primary sensors. IEEE Proceedings-G (Circuits, Devices and Systems). 1992;139(1): 89-98.
9. Soleimani M. Image and shape reconstruction methods in magnetic induction tomography and electrical impedance tomography. Ph.D. thesis, 2005; University of Manchester, Department of Engineering and Physical Sciences, Manchester, England.
10. Gupta S and Loh KJ. Noncontact electrical permittivity mapping and pH-sensitive films for osseointegrated prosthesis and infection monitoring. IEEE Transactions on Medical Imaging. 2017; 36(11): 2193-2203.
11. Gupta S, Loh KJ. Noncontact and noninvasive strain monitoring of osseointegrated prostheses. Proceedings of the 11th International Workshop on Structural Health Monitoring, Stanford, CA, September 12-14, 2017.
12. Adler A, Arnold JH, Bayford R, Borsic A, Brown B, Dixon P, Faes TJ, Frerichs I, Gagnon H, Gärber Y, Grychtol B. GREIT: a unified approach to 2D linear EIT reconstruction of lung images. Physiological Measurement. 2009; 30(6): S35-S55.
13. Evangelidis M, Ma L, and Soleimani M. High definition electrical capacitance tomography for pipeline inspection. Progress in Electromagnetics Research. 2013; 141: 1–15. .
14. Al Hosani E, Zhang M, and Soleimani M. A limited region electrical capacitance tomography for detection of deposits in pipelines. IEEE Sensors Journal. 2015; 15(11): 6089-6099.

Conflicts of Interest

The authors do not have any conflicts of interest.

Human Subjects

No human subjects were used in this study nor were animal experimentations performed.